Photoelasticity of VO_2 nanolayers in insulating and metallic phases studied by picosecond ultrasonics

Ia. A. Mogunov,[1,*] S. Lysenko,[2] F. Fernández,[2] A. Rúa,[2] A. V. Muratov,[3] A. J. Kent,[4] A. M. Kalashnikova,[1] and A. V. Akimov[4]

[1]*Ioffe Institute, 194021 St. Petersburg, Russia*

[2]*Department of Physics, University of Puerto Rico, Mayaguez, Puerto Rico 00681, USA*

[3]*P.N. Lebedev Physical Institute of the Russian Academy of Sciences, 119991 Moscow, Russia*

[4]*School of Physics and Astronomy, The University of Nottingham, Nottingham NG7 2RD, United Kingdom*

(Received 30 July 2020; accepted 11 November 2020; published 14 December 2020)

We use a picosecond ultrasonic technique to evaluate the photoelastic parameters at the wavelength of 1028 nm in epitaxial vanadium dioxide (VO_2) nanolayers grown on c-cut sapphire substrates. In the experiments, we monitor the picosecond evolution of the reflectivity of VO_2 in insulating and metallic phases under the impact of a picosecond longitudinal strain pulse injected into the nanolayer from the side of the substrate. We show that in a 145-nm-thick granular nanolayer, the temporal features of the reflectivity are clearly dependent on the phase state of VO_2, showing the change of the photoelastic parameters upon the insulator-metal transition. Analytical consideration and numerical simulations of the optical response to the picosecond strain pulse show that the temporal evolution of the reflectivity strongly depends on the complex photoelastic parameter. The analysis enables us to obtain the values of the photoelastic parameters in the studied nanolayer in both insulating and metallic phases. We find that for a 145-nm film of VO_2 in an insulating state the imaginary part of the photoelastic constant is negligible. This means that in the insulating phase the strain does not affect the optical absorption of VO_2. In the metallic phase, the photoelastic parameter of VO_2 is found to be similar to that typical for metals with positive real and negative imaginary parts. We further show that the optical response to the strain pulse in the layer consisting of disconnected VO_2 nanohillocks with an average height of 70 nm is governed by their morphology and is different from what is predicted in the plane VO_2 films.

DOI: 10.1103/PhysRevMaterials.4.125201

I. INTRODUCTION

Vanadium dioxide is a strongly correlated material well known for its first-order insulator-to-metal phase transition (IMT), discovered by Morin in 1959 [1]. In its low-temperature phase, VO_2 is a monoclinic correlated insulator with a band gap of 0.6 eV [2,3]. When heated above 340 K, the gap collapses resulting in up to 5 orders of magnitude increase in conductivity [4] as well as drastic changes of optical spectra in the infrared region [5]. The IMT is accompanied by a structural phase transition (SPT), changing VO_2 from monoclinic M1 phase to tetragonal R phase [6,7]. Phase transition in VO_2 can also be triggered on a femtosecond timescale by light pulses with photon energy above the material's band gap when optical fluence exceeds a threshold of a few mJ/cm^2 [8], and is usually realized in thin films and other nanostructures since bulk VO_2 samples cannot withstand repetitive IMT without fracturing [9]. Ability of VO_2 to switch between different electronic and structural phases under various stimuli enables prospective applications of VO_2 films and nanostructures, including optical switches [10], optical memories [11], memristive devices [12,13], photoinduced actuators [14–16], smart windows [17], THz modulators [18–20], optoacoustic transducers [21], and others [22,23].

The coexistence of electronic and lattice changes during the phase transition indicates the importance of electron-phonon coupling in VO_2. As a result, the complex mechanisms behind the IMT in this material are still controversial. In order to achieve complete understanding and to take full advantage of the phase transition in VO_2 for its multiple prospective applications, a thorough description of its properties in both phases is required. Although the optical and electronic properties of VO_2 have been studied in detail (for a review see, e.g., Ref. [2]), there are only few works where an effort has been made to evaluate its elastic and photoelastic [24–28] properties. Photoelastic properties of the material are characterized by the fourth order photoelastic tensor which connects its permittivity and strain tensors. The reduced complex photoelastic constant P for isotropic media is often used [29–31]:

$$P = \frac{\partial N}{\partial \varepsilon} = \frac{\partial n}{\partial \varepsilon} + i\frac{\partial \kappa}{\partial \varepsilon} = p + iq. \tag{1}$$

where $N = n + i\kappa$ is the complex refractive index and ε is the strain. The value of P depends on the optical wavelength and may increase dramatically for photon energies near the band gap E_g and other singularities in the electron spectrum [32]. In this simple case, p and q reflect the dependencies of n and κ, respectively, on photon energy, and the knowledge of P provides information about the electronic band structure of the material. However, the deformation potential is not the

*mogunov@mail.ioffe.ru

only mechanism which defines the value of P and often more sophisticated models are required to explain photoelasticity in solids [33].

The photoelastic effect may be studied by applying uniaxial static stress to the material in various crystallographic directions and monitoring the changes of the refractive index [32]. This direct method provides comprehensive information about all elements of the photoelastic tensor, but is limited to bulk single-crystal specimens. Unfortunately, bulk VO_2 crystals often fracture under stresses generated during the IMT. Moreover, since most of the innovative VO_2 applications require nanofabricated devices, and operate on ultrafast timescale, a technique is necessary which may access photoelastic properties on such spatial and temporal scales. An approach to study the photoelastic effect in thin films and nanostructures is provided by picosecond ultrasonics (PU), which applies dynamical strain, e.g. a picosecond strain pulse, and monitors the temporal evolution of the strain-induced changes in the reflection or transmission of the probe light [34,35]. In addition to enabling studies of photoelastic properties of thin films and nanostructures, this technique is efficient even when the strain-induced changes of optical properties are very small, which is the case for photon energies far from the band gap and other electronic band structure singularities.

The present paper aims to determine experimentally the photoelastic properties of nanosized VO_2 and their change upon IMT. We report on PU measurements in two VO_2 epitaxial nanolayers on c-cut sapphire substrates, performed both above and below the IMT temperature. Picosecond strain pulses are generated in an Al transducer and, after propagation through the sapphire, are injected into the VO_2 nanolayer. The photoelastic effect in VO_2 is monitored by measuring with picosecond temporal resolution the strain-induced changes in the intensity of a probe laser pulse reflected from the nanolayer. We observe well-pronounced changes of the detected signal when the VO_2 nanolayer experiences IMT, showing that the photoelastic effect changes upon the transition. We perform simulations of the photoelastic response of VO_2 which show that for relatively thick ($>$100 nm) VO_2 nanolayers the temporal shape of the detected signal strongly depends on the value of P. Such dependence allows us to estimate the absolute values of P in VO_2 in insulating and metallic phases.

The paper is organized as follows. In Sec. II, we characterize the VO_2 samples used in the study and describe the PU experimental setup. Section III presents the experimental results. Section IV gives the theoretical background for the analysis of photoelastic effect and presents the results of numerical calculations for the VO_2 nanolayer in insulating and metallic phases. In Sec. V, we compare experimental results with calculations, estimate photoelastic parameters of VO_2 in insulating and metallic phases and discuss the origin of photoelasticity in VO_2. Section VI summarizes our work and discusses the implementations of the obtained results.

II. EXPERIMENT

A. Samples

The samples studied are two VO_2 epitaxial nanolayers grown on 350-μm-thick c-cut Al_2O_3 substrates by pulsed laser deposition technique [36]. The nanolayers were fabricated in an oxygen and argon atmosphere under a total pressure of 50 mTorr, measured with a diaphragm capacitance sensor, and with Ar and O_2 gas flows independently adjusted to 10 and 15 SCCM respectively, with mass flow controllers. Background pressure in the chamber was of order 10^{-6} Torr. A rotating metallic vanadium target was ablated by a pulsed KrF excimer laser Lambda Physik Compex 110, wavelength 248 nm, 20 ns pulse duration, 10 pulses/s, and 4 J/cm^2 fluence. During deposition, substrate temperature was kept at 550 °C by a resistive heater with proportional-integral-differential (PID) feedback controller. The VO_2 layers grown on c-cut Al_2O_3 are known to have the monoclinic M1 structure at room temperature, with $[020]_{M1}$ crystallographic axis of VO_2 perpendicular to the (001) Al_2O_3 plane [36]. Azimuthal XRD scans reveal threefold in-plane twinning characteristic for epitaxial VO_2 nanolayers on c-cut sapphire substrates [4,36].

Atomic force microscopy (AFM) images of the studied VO_2 nanolayers shown in Figs. 1(a) and 1(b) reveal the granulated structure of the VO_2 films. The granulated structure is common for VO_2 epitaxial nanolayers grown on c-cut Al_2O_3 and is due to a large in-plane lattice mismatch with the substrate [7,37]. The formation of grains, twinning, and domain-matched growth result in the relaxation of the built-in strain [37]. There are no significant gaps between the grains in the nanolayer for which the AFM image is shown in Fig. 1(a). The average thickness of the nanolayer is $l = 145$ nm with $<10\%$ uncertainty, as obtained from ellipsometry measurements. The height deviation histogram obtained from the AFM image [see the inset in Fig. 1(a)] is symmetrical with 40 nm root mean square roughness. The mean lateral size of the granules is of $\sim$250 nm. The AFM image of the second sample [Fig. 1(b)] shows that the grains are clearly separated from each other, and this VO_2 nanolayer may be considered as a set of isolated nanohillocks with height of 50–90 nm and diameter of 150–350 nm. Below we refer to these two samples as a 145-nm film and nanohillocks, respectively.

The IMT temperature T_c in the studied VO_2 nanolayers was determined from the temperature hysteresis of the optical reflectivity R_0 at wavelength $\lambda = 1028$ nm [see Fig. 1(c)]. The transition temperatures for the 145-nm film and nanohillocks are $T_c = 343$ and 340 K, respectively, and agree with the value of 340 K in the bulk VO_2 [1], which is a manifestation of low built-in strain in the studied samples [38].

B. Picosecond ultrasonics setup and strain pulse characteristics

The PU experimental schematics is shown in Fig. 1(d). A polycrystalline aluminum film, which serves as optoacoustic transducer [34], is deposited on the back side of the sapphire substrate by magnetron sputtering. The Al film thickness $h \sim 140$ nm was measured in acoustic echo experiments, as described elsewhere [30,31,34]. The Al film is excited by the pump laser pulses from a Yb-doped $KGd(WO_4)_2$ regenerative amplifier laser source emitting 170 fs pulses with a central wavelength 1028 nm and a repetition rate of 100 kHz. The pump beam is focused on the spot with diameter $\sim$60 μm with maximum fluence $W \sim 20$ mJ/cm^2. As a result of pump

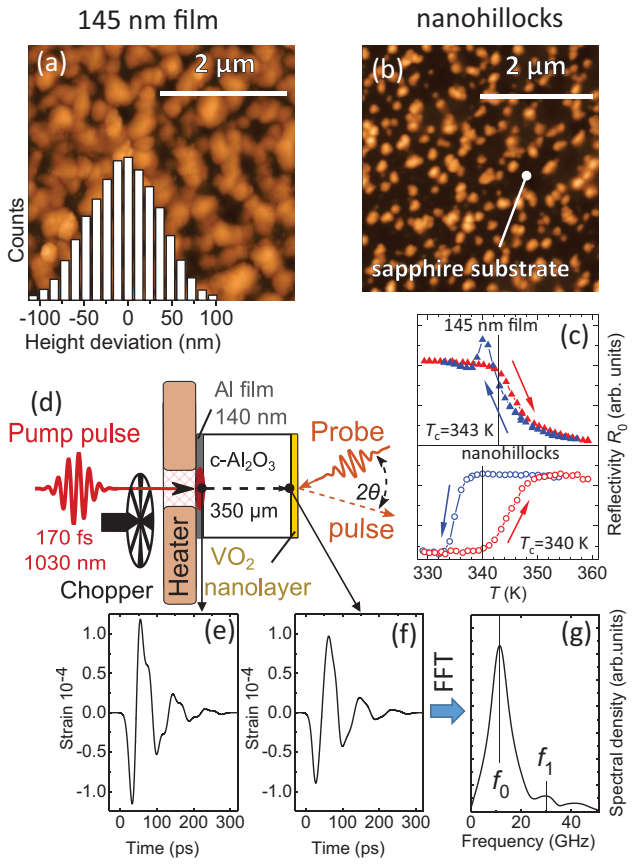

FIG. 1. The AFM images of the studied VO_2 nanolayers: (a) a 145-nm granulated film, inset shows the height distribution histogram based on the image; (b) an ensemble of nanohillocks. (c) Temperature dependence of the reflectivity R_0 on $\lambda = 1028$ nm across the insulator/metal phase transition for 145-nm film (upper) and nanohillocks (lower). T_c for the samples are shown with vertical lines. (d) Schematic of the picosecond ultrasonics experimental setup. (e) The strain pulse as emitted from the Al film into sapphire substrate and (f) upon approaching the VO_2 layer. (g) FFT amplitude of the strain pulse shown in (f).

excitation and thermoelastic effect in Al film a bipolar longitudinal picosecond strain pulse with duration ∼20 ps and amplitude up to $\sim 10^{-3}$ is generated [39–41]. The strain pulse undergoing multiple reflections at Al/Al_2O_3 and Al/air interfaces is injected into the sapphire substrate. Penetration depth in aluminum for $\lambda = 1028$ nm is of ∼9 nm, and pump pulses do not reach the substrate and the VO_2 film.

The amplitude of the strain pulse injected into the sapphire substrate is reduced due to acoustic mismatch between Al and Al_2O_3. For the used fluences W, no acoustic nonlinearities were observed, so we estimate the maximum amplitude of the strain pulse in sapphire to be $\sim 10^{-4}$ and the corresponding calculated temporal profile is shown in Fig. 1(e). The injected strain pulse travels through the 350-μm-thick sapphire substrate with longitudinal sound velocity 11230 m/s and reaches the VO_2 nanolayer in $t_0 = 32$ ns. During the propagation in the sapphire substrate, the strain pulse evolves due to damping and phonon dispersion [42]. The temporal profile $\varepsilon_0(t)$ of the strain pulse which reaches VO_2 nanolayer is shown in Fig. 1(f). For the used substrate temperatures, the temporal profile $\varepsilon_0(t)$ only slightly depends on the fluence W. The fast Fourier transform (FFT) of the strain pulse entering VO_2 is shown in Fig. 1(g). It consists of a broad peak centered at $f_0 \sim 10$ GHz and a weak satellite at $f_1 \sim 30$ GHz. The values of f_0 and f_1 are consistent with the first two vibrational resonances of the Al transducer with a thickness $h = 140$ nm [43]:

$$f_j = \frac{(2j+1)s_{\mathrm{Al}}}{4h}, \tag{2}$$

where $s_{\mathrm{Al}} = 6400$ m/s is the velocity of longitudinal sound in Al.

The strain pulse injected into the VO_2 nanolayer modulates the permittivity of the VO_2 and changes the reflectivity $R(t)$ of the probe pulse. The probe is incident at the VO_2 nanolayer at an angle $\theta = 30^\circ$ and is focused to a spot with diameter 25 μm exactly opposite to the pump spot at the surface with the Al film. The probe pulse originating from the same laser source is delayed by t with respect to the pump pulse arriving at t_0 by means of a motorized optomechanical delay line. The fluence of the probe beam is less than 0.1 mJ/cm^2 which is well below the threshold for photoinduced phase transition in VO_2 [2,8,21,28]. The intensity $R(t)$ of the reflected probe beam is measured as a function of the time delay t using the balanced photodetection scheme with a reference beam split from an incident probe beam to reduce laser source noises. We use an optomechanical chopper to modulate the pump beam and a lock-in amplifier to extract the temporal evolution of the strain-induced change $\Delta R(t)$ in the reflectivity signal.

The sample is attached to a copper plate with an electric heater [Fig. 1(d)]. The thermal contact is provided by silver paste and the sample temperature is monitored by a thermocouple. The heater allows measurements in a temperature range $T = 295$–400 K which covers the IMT temperature for both VO_2 samples.

III. EXPERIMENTAL RESULTS

Figure 2 shows the normalized experimental temporal evolutions $\Delta R(t)/R_0$ of the strain-induced relative reflectivity changes and their FFTs at two temperatures, $T = 295$ and 355 K, which are below and above the IMT transition, respectively. Colored lines correspond to results obtained for various fluence values W in the case of the 145-nm VO_2 film. Note the independence of $\Delta R(t)/R_0$ shape on W, confirming linear acoustic regime. The black lines show examples for the signal in the VO_2 nanohillocks sample. All signals $\Delta R(t)/R_0$ have oscillatory behavior dominated by an oscillation with ∼100 ps period superimposed on lower-amplitude higher frequency components [see Figs. 2(a) and 2(b)]. The FFT spectra shown in Figs. 2(c) and 2(d) consist of two spectral peaks located in the same frequency ranges as those in the FFT spectrum of the simulated incident strain pulse [Fig. 1(g)]. Namely, the strong peak is centered close to $f_0 \sim 10$ GHz and the weaker one to $f_1 \sim 30$ GHz.

As can be seen from the comparison of the traces in Figs. 2(a) and 2(b), the temporal shape of $\Delta R(t)/R_0$ in the 145-nm VO_2 film depends on whether the sample is in the insulating or metallic phase. The most striking difference is

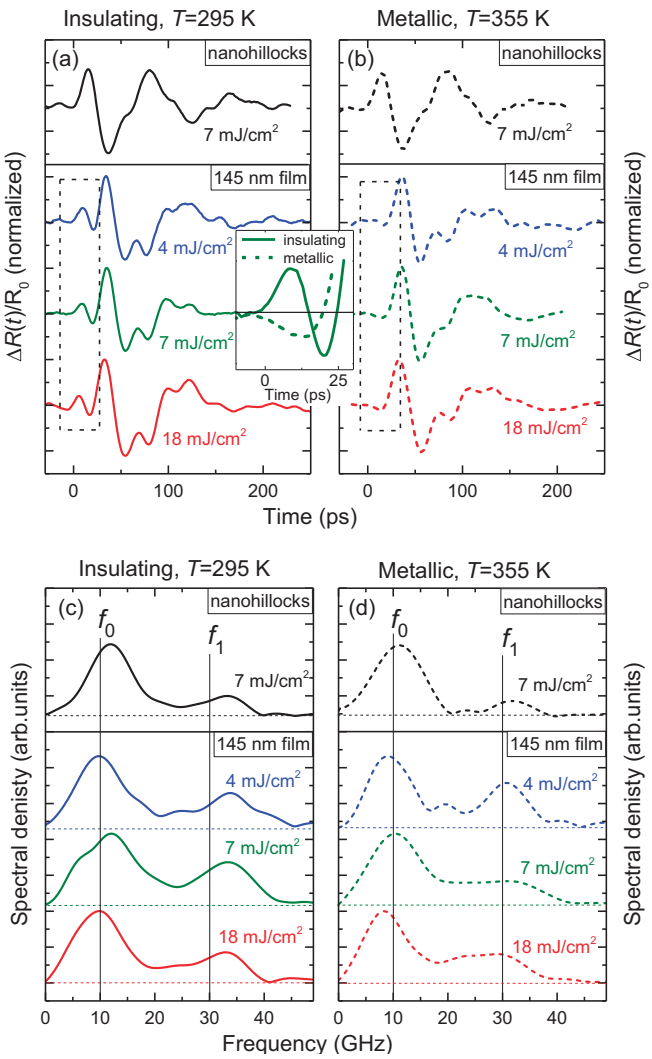

FIG. 2. Normalized temporal profiles of the reflectivity signals $\Delta R(t)/R_0$ [(a) and (b)] and their FFTs [(c) and (d)] measured for two temperatures, $T = 295$ [(a) and (c)] and 355 K [(b) and (d)], and various pump excitation fluences W. Upper panels correspond to the VO_2 nanohillocks and lower ones to the 145-nm VO_2 film. The dashed rectangles in (a) and (b) mark the time interval where the temporal shape strongly depends on the phase, insulating or metallic, of 145-nm VO_2 film. Inset in (a) and (b) shows the zoomed fragments of the signals in insulating (solid line) and metallic (dashed line) phases in 145-nm layer at $W = 7$ mJ/cm^2.

observed at early time interval 0–30 ps marked in Figs. 2(a) and 2(b) by dashed rectangles and enlarged in the inset of Fig. 2 for one of the cases. When VO_2 is in its insulating fluences, $\Delta R(t)/R_0$ changes its sign in this time interval showing an oscillation with a period ~30 ps. After that $\Delta R(t)/R_0$ increases towards the maximum observed at $t = 34$ ps. In the metallic phase, $\Delta R(t)/R_0$ shows only a small dip in the time interval 0–30 ps preceding the positive peak. In contrast to the 145-nm film, for the VO_2 nanohillocks sample, we do not observe a significant difference in temporal shapes for $\Delta R(t)/R_0$ measured in insulating and metallic phases [compare black curves in Figs. 2(a) and 2(b)].

The difference in $\Delta R(t)/R_0$ response in insulating and metallic phases for the 145-nm VO_2 film is the main experimental result we emphasize here. In particular, the difference of $\Delta R(t)/R_0$ in insulating and metallic phases seen at early times of 0–30 ps is observed for all fluences W used in these experiments. Importantly, this difference is found to be independent of position of the pump-probe spot on the sample. This indicates that the observed difference is not related to any inhomogeneities in the VO_2 nanolayer or Al transducer. Therefore, from these results, we conclude that the difference in $\Delta R(t)/R_0$ in the insulating and metallic phases is another manifestation of the IMT in VO_2, which, to the best of our knowledge, was not recognized in numerous previous studies of the optical properties of VO_2. To unveil the physical processes and material parameters responsible for the difference in the temporal evolutions of $\Delta R(t)/R_0$ in insulating and metallic phases, we simulated $\Delta R(t)/R_0$ for VO_2 films and analyzed how it depends on the optical, acoustical and photoelastic parameters of the film. This analysis and comparison with the experimental data are given in the next Secs. IV and V.

IV. ANALYSIS

In this section, we describe the general properties of the PU signals $\Delta R(t)/R_0$ and their spectrum in absorbing films. Two approaches are commonly employed for simulations of $\Delta R(t)/R_0$: analytical and numerical. For the case of the films with complex refractive index and complicated multilayer structures the numerical methods, based on transfer matrix formalism, are more productive, while the analytical approach remains useful if one needs to single out different contributions which govern the PU signal. In this section, we consider an idealized case of a homogeneous smooth film. Application of the results of such an analysis to the realistic VO_2 layers is discussed in Sec. V.

A. Picosecond ultrasonic signal. Analytical approach

We consider the PU signal detected in the scheme shown in Fig. 1(d) when the probe light with wavelength λ is incident on a film with a thickness l, complex refractive index $N = n + i\kappa$, and photoelastic constant $P = p + iq$ given by Eq. (1). The film is deposited on a transparent substrate with a real refractive index n_0. The equation for the relative changes in the reflectivity $\Delta R(t)/R_0$ induced by the longitudinal strain pulse ($z = 0$ at the interface with air) is given in Ref. [44] and may be written in a form (see Appendix):

$$\frac{\Delta R(t)}{R_0} = 4\mathrm{Im}\left\{A_N\left[(N+P)\int_0^l \varepsilon(t,z)dz + \frac{1}{2}P\int_0^l \varepsilon(t,z)\left(r_{12}e^{2ik_1(l-z)} + \frac{1}{r_{12}}e^{-2ik_1(l-z)}\right)dz\right]\right\}, \quad (3)$$

where r_{12} is the Fresnel reflection coefficient for the electric field amplitudes at the film/substrate interface, $k_1 = 2\pi N/\lambda$ is the wave vector of light inside the film, and A_N is a complex coefficient dependent on k_1 and l, but independent of strain (see Appendix).

TABLE I. Elastic and optical parameters of VO_2 and the substrate at λ=1028 nm used in the calculations

Vanadium dioxide $[020]_{M1}$	
Density (kg/m^3)	4570
LA Sound velocity, s_{VO_2} (m/s)[a]	7850 ± 800
Refractive index (insulating), N_{ins}	$(1.91 \pm 0.06) + i(0.8 \pm 0.01)$
Refractive index (metallic[b]), N_{met}	$(1.50 \pm 0.05) + i(1.59 \pm 0.02)$
Sapphire substrate [001]	
Density (kg/m^3)	3950
LA sound velocity (m/s)	11230
Refractive index, n_0	1.8

[a]Calculated from experimentally measured VO_2 phonon dispersion curves [26].
[b]Estimated by scaling the results in Ref. [45] to the measured value of N_{ins}.

Equation (3) includes two terms with integrals. The first term originates from the modulation of the interface displacements and, respectively, the film thickness. The integral in this term is a real function of t. As a result, optical parameters N and P affect the sign and the amplitude, but do not affect the temporal shape of this contribution. The second term in Eq. (3) originates from the photoelastic effect. For this contribution, optical parameters N and P can affect the temporal shape of $\Delta R(t)/R_0$ if their imaginary parts are nonzero. These qualitative conclusions are verified for a case of VO_2 using the numerical calculations and are helpful in finding the values of P from the measured signals.

B. Numerical calculation

We performed numerical calculations of $\Delta R(t)/R_0$, taking into account both contributions described above in Sec. IV A, using codes based on MATLAB software. First, we calculate the strain pulse profile after its passage through the substrate. Temporal profile of the strain pulse at the transducer/sapphire interface is shown in Fig. 1(e). Evolution of the strain pulse upon propagation in sapphire is obtained by solving the Korteweg-de-Vries-Burgers equation [42] in the spectral domain. The resulting temporal profile $\varepsilon_0(t)$ at the sapphire/film interface is shown in Fig. 1(f). As a second step, the temporal and spatial distributions of strain and atomic displacement in the film are calculated following the strain pulse $\varepsilon_0(t)$ entering the film. The reflections of the acoustic wavepacket at the film/substrate and film/air interfaces are taken into account based on the acoustic mismatch parameters of sapphire and VO_2. Finally, the optical reflectivity change $\Delta R(t)/R_0$ is calculated using the transfer matrix formalism in a film with known distributions of strain $\varepsilon(t, z)$ and atomic displacement $u(t, z)$, complex refractive index N and photoelastic parameter P.

The parameters used in the calculations are given in Table I. Two values of N corresponding to the insulating and metallic phases of VO_2 were used. The value of N in the insulating phase was measured by ellipsometry at room temperature, and further scaling to N in metallic phase was made using previous works [45]. The complex photoelastic parameter $P = p + iq = \rho_P \exp(i\varphi)$ was varied in a range of $\rho_P = [0 \dots 9]$, $\varphi = [0 \dots 2\pi]$. It was found that the temporal shape of $\Delta R(t)/R_0$ depends on P. To illustrate this dependence and to enable the comparison with experimental results it is convenient to analyze the FFT amplitude spectral densities S in two frequency ranges 1–24 and 25–51 GHz presented as color plots versus P in Figs. 3(a)–3(d).

The dependencies of S possess minima shown as blue stripelike regions in Figs. 3(a)–3(d). The position and orientation of the blue stripe depends on the phase of VO_2 (insulating or metallic) and the spectral range, which is a result of the P-dependent temporal profile of the reflectivity change. Such dependence of $\Delta R(t)/R_0$ and its spectra on P stems from photoelastic effect, which follows from the discussion of Eq. (3) in Sec. IV A. From the data shown in Fig. 3 one can see that varying P in a particular phase of VO_2, i.e., when N is fixed, results in noticeable change of the relative contributions from the low- and high-frequency spectral components of $\Delta R(t)/R_0$. This is clearly seen from the examples of calculated temporal traces illustrated on Figs. 3(e)–3(j) for various values of P and N. For instance, panels (e), (h), and (i) demonstrate examples where high frequency oscillations are well pronounced. On the contrary, panels (f), (g), and (j) are examples when low frequency oscillations are dominant. The relative high- and low-frequency contributions change for the same P but different N values [compare the panels (g), (h) and (i), (j)].

Therefore, analyzing the temporal signals $\Delta R(t)/R_0$ and their FFTs, one should be able to determine the range of values of P allowing description of the main features of the experimental data in the insulating and metallic phases of the studied films. The details of the procedure used in this work to find the values of P for the studied samples are given next, in Sec. V.

Finally, we note that the dependence of S on P becomes less pronounced with decreasing film thickness. For thin films with $l \ll \lambda$ and $l \ll s_{VO_2}(d\varepsilon/dt)^{-1}$, the temporal shape of $\Delta R(t)/R_0$ remains the same for all values of P and matches the derivative of the strain pulse $\varepsilon_0(t)$ entering the film. However, the sign (i.e., the phase of the oscillations) of $\Delta R(t)/R_0$ for such thin films is still sensitive to P since it is governed exclusively by the complex values of N and P, as can be seen from Eq. (3).

V. DISCUSSION

The analysis presented in Sec. IV paves a way to obtain the values of P in the insulating and metallic phases from the experimentally measured $\Delta R(t)/R_0$. Before performing the comparison between the measured and simulated signals we have to note the difference between VO_2 nanolayers studied experimentally and the idealized case used in the model simulations. The primary difference is that the real VO_2 nanolayers are granulated and cannot be considered as ideal plane films. The 145-nm film consists of granules with height variations of $\Delta l = \pm 40$ nm and mean lateral size of $\sim$250 nm [see Fig. 1(a)], which is the order of the wavelength, $\sim$300 nm, for 30 GHz phonons and optical wavelength λ/n. Thus, phonon scattering and diffraction at the free surface of VO_2 partially

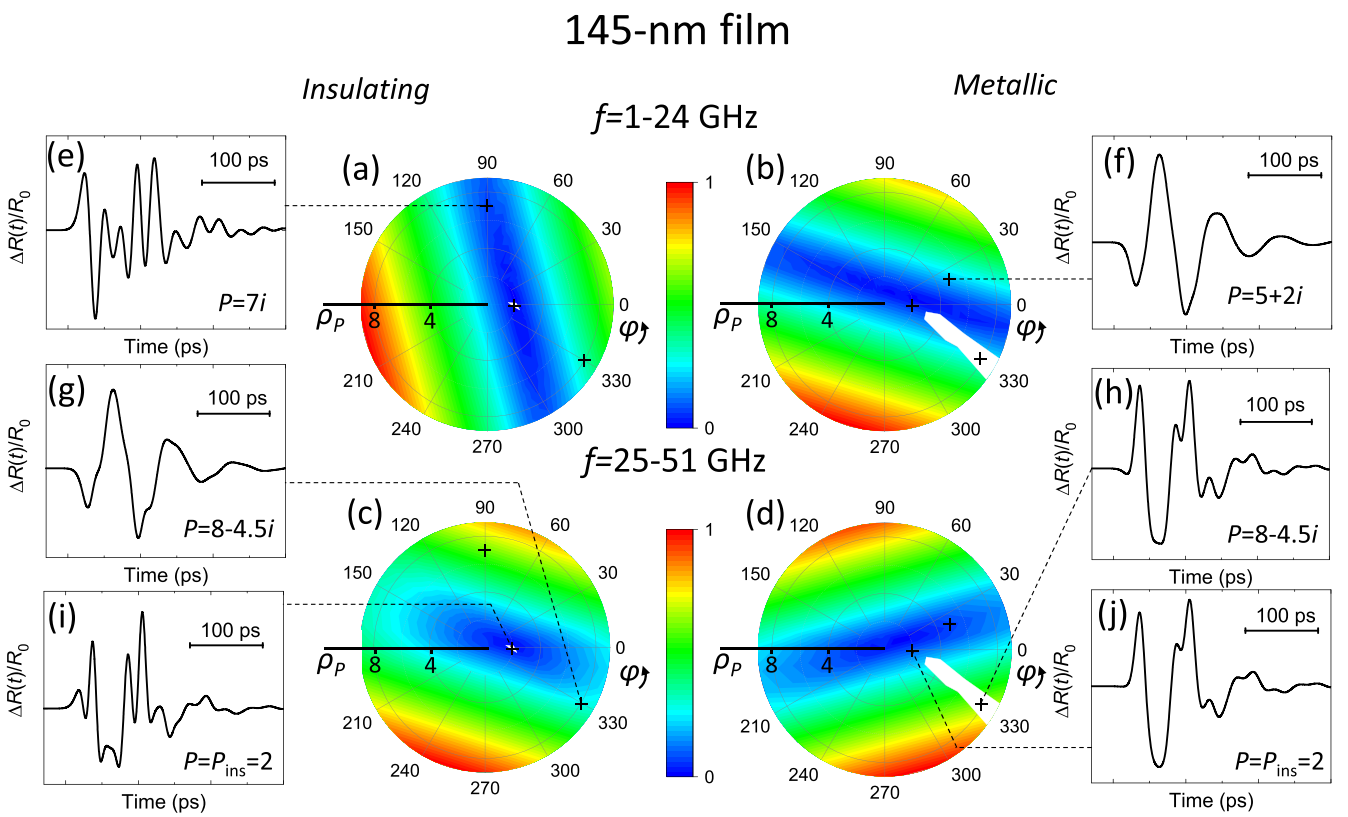

FIG. 3. Simulation results for a range of photoelastic constant $P = \rho_P e^{i\varphi}$, $0 < \rho_P < 9$, $0 < \varphi < 360^\circ$, in insulating (left part) and metallic (right part) phases of VO_2. (a)–(d) Spectral densities S of simulated temporal profiles $\Delta R(t)/R_0$ for two spectral ranges: f=1–24 [(a) and (b)] and 25–51 GHz [(c) and (d)]. White regions mark the range of P showing the best agreement with the experiments including uncertainties of calculation parameters. Black crosses indicate a set of selected P values for which simulated $\Delta R(t)/R_0$ are shown.

destroys the coherence of the reflected phonons in the wave packet of the strain pulse. Such behavior results in damping of high-frequency spectral components in the detected PU signal [46]. Importantly, the phonons scattering and diffraction start to affect the PU signal at delays $t > \tau_0$, where τ_0 is the phonon propagation time from the film/substrate interface to the free surface. For the 145-nm film, $\tau_0 \sim l/s_{VO_2} = 17$ ps where $s_{VO_2} = 7850$ m/s is VO_2 longitudinal sound velocity in corresponding direction (see Table I). However, the damping becomes evident at longer times, depending on the rise time of the leading edge of the input strain pulse $\varepsilon_0(t)$, which is ~30 ps in our experiments. This qualitative consideration leads us to the conclusion that the comparison of the measured and simulated $\Delta R(t)/R_0$ for 145-nm film is valid for t not exceeding a few tens of picoseconds.

Figure 4 shows the normalized measured and simulated signals $\Delta R(t)/R_0$ and their FFTs. The solid blue lines correspond to the simulations performed for the film with $l = 145$ nm. The dotted rectangles in Fig. 4(a) mark the characteristic temporal feature at early times $t < 30$ ps in the signals in the insulating phase. This feature is clearly reproduced in the simulated signal. Good agreement is observed for $P_{ins} = 2$, for which both general shape and relative amplitudes of the temporal peaks of the normalized signal match the experimental result. The high-frequency temporal feature is quite sensitive to the photoelastic constant, as indicated by a very narrow P-range [see white region in Figs. 3(a) and 3(c)] for which the relative amplitudes for this time interval remain within 30% from experimentally obtained values taking into account uncertainties of the calculation parameters (Table I). Similar criteria used for comparison between experimental and simulated $\Delta R(t)/R_0$ in the metallic phase leads to a significantly larger range of appropriate P values [see white region in Figs. 3(b) and 3(d)]. The calculated $\Delta R(t)/R_0$ corresponding to the best agreement with the experiment is shown as a solid blue curve on Fig. 4(b), for P_{met}=3−0.5i. Note the excellent agreement with experiment (black curve) in reproducing a small dip at $t \sim 20$ ps.

For longer times $t > 45$ ps, the amplitude of high-frequency oscillations in the measured $\Delta R(t)/R_0$ is damped compared to the simulated signals in both insulating and metallic phases. To show the effect of inhomogeneities at that time interval we have performed the averaging of $\Delta R(t)/R_0$ over a range of thicknesses around $l = 145$ nm. The weight of $\Delta R(t)/R_0$ for each thickness in the sum was included in accordance with the height deviation histogram [see inset in Fig. 1(a)]. Such modeling assumes that the lateral size of the granules and other inhomogeneities is much larger than the phonon and photon wavelengths. Although this condition is not satisfied in the studied 145-nm film, even such a simple model shows qualitatively how the films inhomogeneities modify $\Delta R(t)/R_0$. The simulated averaged $\Delta R(t)/R_0$ for both phases of VO_2 and corresponding FFTs are shown by dashed blue lines in Fig. 4. For the insulating phase, the characteristic

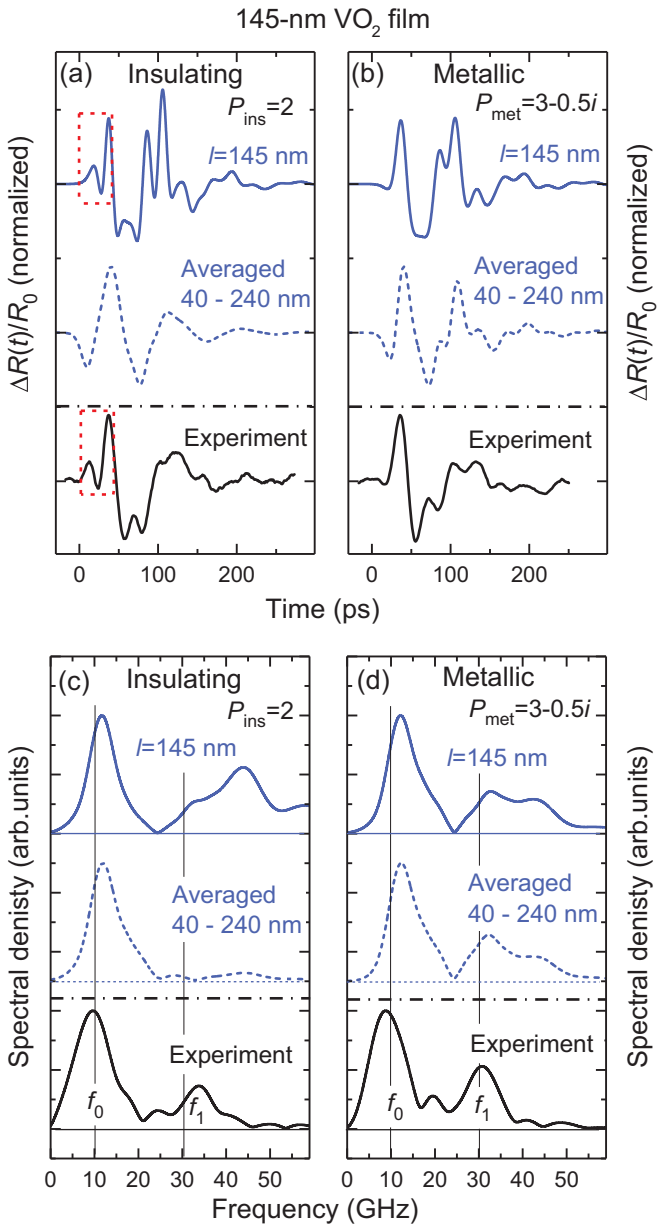

FIG. 4. The measured (black lines) and simulated (blue lines) PU temporal signals $\Delta R(t)/R_0$ [(a) and (b)] and their FFTs [(c) and (d)] for 145-nm VO_2 film in insulating [(a) and (c)] and metallic [(b) and (d)] phases. The blue solid lines correspond to the simulations for the smooth film with 145-nm thickness. Blue dashed lines are the result of averaging over the layers with various thicknesses 40–240 nm.

high-frequency feature at early times $t < 30$ ps disappears, but $\Delta R(t)/R_0$ at longer times $t > 45$ ps, as well as the FFTs, show a good agreement with the experimental signal. For the metallic phase, the agreement between the averaged simulated and experimental temporal signals $\Delta R(t)/R_0$ and their FFTs is reasonable in the whole temporal range.

Based on the comparison between the experimental and simulated data, we are able to draw the following conclusions about the values for the reduced photoelastic constants P.

(i) Their values are different in insulating and metallic phases;

(ii) $P_{\rm ins}$ in the insulating phase has a negligible negative imaginary part $|q_{\rm ins}| < 0.05$ which is much less than a real part $p_{\rm ins} = 2$;

(iii) In the metallic phase, there is an ambiguity in defining $p_{\rm met}$ and $q_{\rm met}$. The experimental data can be described by any set of $p_{\rm met}$ and $q_{\rm met}$ along the ray [Fig. 3(a)], which is described by an equation $q = -0.8p + 1.9$, starts with the point $P_{\rm met} = 3 - 0.5i$ and expands to larger magnitudes of p and q;

(iv) The absolute values of p and q in the metallic phase are of the same order of magnitude;

(v) In the metallic phase, the sign of p is positive while the sign of q remains negative.

The small value of the imaginary part $|q| \ll |p|$ in the insulating phase means that compressing a VO_2 nanolayer in the out-of-plane direction does not have a strong effect on the optical absorption. This result cannot be explained in the frame of deformation potential mechanism for the photoelastic effect [40], for which $P = \Xi \partial N/\partial E$, where Ξ is deformation potential and E is photon energy. Ellipsometry measurements of the studied 145-nm layer show that in the proximity of excitation wavelength $\lambda = 1028$ nm $|\partial n/\partial E| \sim |\partial \kappa/\partial E|$ in insulating phase, and assuming deformation potential mechanism we get $|p| \sim |q|$ which does not agree with the experimental results. Apparently, a more sophisticated analysis, like presented in Ref. [47], would have to be used in order to explain the measured values for P in the insulating phase. The values for P in the metallic phase are included in white regions in Figs. 3(b) and 3(d) stretching out to infinite magnitudes of P. It is safe to assume that the physically realized values are closer to the tip of the white region, meaning that the magnitude of P must be limited. With such a constriction, the values for $P_{\rm met}$ are quite common and similar to the values measured in other metals [30,31].

Finally, we discuss the results for VO_2 nanohillocks. The simulations show that for film thickness $l = 70$ nm, which is equal to the average height of nanohillocks, the situation is very close to the thin film limit, and the temporal shape of $\Delta R(t)/R_0$ does not depend on P except for the phase, 0 or π, of the oscillations. The results for the simulations in insulating and metallic phases are shown by the solid blue lines in Fig. 5 together with the experimental black curves. The values of P used in the simulations are the same as obtained from the comparison of calculated and experimental signals for the 145-nm film, namely $P_{\rm ins}$ and $P_{\rm met}$. One can see that the simulated signals show the oscillations in antiphase to the measured $\Delta R(t)/R_0$. Nevertheless, the temporal shapes of the simulated and measured signals agree well, as may be seen comparing the black solid and dashed red lines in Fig. 5. The agreement of the experimental and calculated shapes in Fig. 5 also means that the modelled strain pulse shape agrees well with the real one since for such a thin layer the shape of $\Delta R(t)/R_0$ is proportional to a derivative of the strain pulse $\varepsilon_0(t)$ (see Sec. IV B). However, the difference in sign means that the values of P obtained from simulations are different in the two samples. The independence of the temporal shape of P for $l = 70$ nm does not allow us to obtain the value of P as accurately as for the 145-nm film. We may only conclude that in the notation of polar coordinates presented in Sec. IV B, $\rho_P > 2$, $150^\circ < \varphi < 285^\circ$ and $\rho_P > 4$, $180^\circ < \varphi < 300^\circ$ in

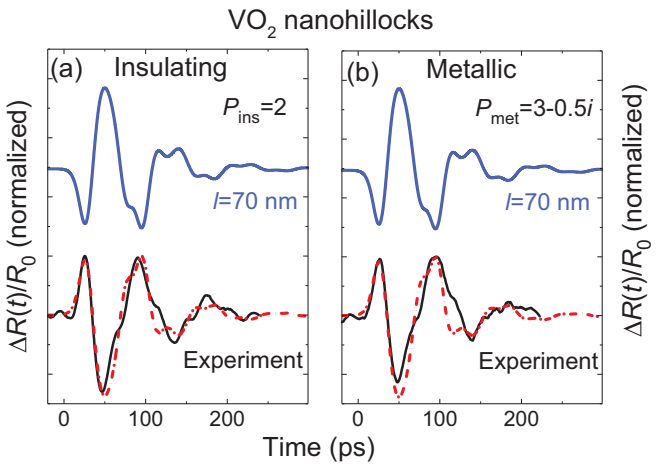

FIG. 5. The PU temporal signals $\Delta R(t)/R_0$ for VO_2 nanohillocks in insulating (a) and metallic (b) phases. The black lines correspond to the measured $\Delta R(t)/R_0$ while the blue lines correspond the simulation results for 70-nm VO_2 film with the same values of P for both phases of VO_2, as in Fig. 4. The dash-dotted red lines are the inverted simulated curves.

insulating and metallic phases, respectively. The difference for the values of the reduced photoelastic parameters P in the two studied samples points at different phonon dynamics in these samples. Indeed, the nanohillocks are isolated on the substrate, and the compression in z direction leads to tension in x and y directions. Thus the analysis of photoelasticity for nanohillocks requires taking into account the full photoelastic tensor instead of reduced isotropic photoelastic constant P. Such analysis requires more sophisticated approaches [48] and controlled shape of VO_2 nanohillocks, which is the prospective task for further investigations.

VI. CONCLUSIONS

To conclude, we have used the picosecond ultrasonic technique to study, experimentally, the photoelastic properties of VO_2 nanolayers with different morphologies, in the insulating and metallic phases. Theoretically we showed that in VO_2 films with thickness more than ~100 nm, the temporal shape of the detected photoelastic signal depends on the value of the reduced complex photoelastic constant. This allowed us to obtain its value from the comparison of theoretical and experimental results. In the insulating phase, the imaginary part of the photoelastic constant is negligible and does not agree with the deformation potential model for photoelastic effect in VO_2. The granulated structure of VO_2 nanolayers in the samples results in the effects of inhomogeneities and damping of high-frequency features in the measured photoelastic signals. There is a dependence of photoelasticity on whether the granules are closely packed in a film or isolated as nanosized grains on the substrate surface. Our experiments show that for closely packed granules, it is possible to make a direct comparison between the photoelastic signals obtained experimentally and simulated for a plane film with thickness corresponding to the average thickness of the studied VO_2 nanolayer.

Our first study of photoelasticity in VO_2 nanolayers paves a way for further investigations of VO_2 nanostructures using picosecond ultrasonics. The knowledge of all elements of the photoelastic tensor would help to understand the electronic properties of this unique material and the changes upon IMT, thus contributing to the debate about the nature of the various phases of VO_2. To obtain complete information about the photoelastic tensor, it is necessary to study monocrystalline VO_2 applying compressive and shear elastic perturbations in various crystallographic directions which is a prospective for further study. For nanostructured VO_2-based devices, however, knowledge of the reduced photoelastic constant in the out-of-plane direction may be already useful for careful consideration of photoelastic effect as well as for effective control of light-strain interaction. For VO_2 nanostructures, the photoelastic effect becomes apparent in recent experiments with ultrafast photoinduced phase transitions [28]. In practice, the photoelastic effect in VO_2 can be exploited via picosecond ultrasonics for ultrafast manipulation of light. Ultrafast optical experiments with VO_2 embedded in photonic crystals [49] show the prospect of high efficiency of such modulation technique.

ACKNOWLEDGMENTS

We thank V. Gusev for fruitful discussions. Ellipsometry was performed by the equipment of the Shared Facility Centers of Lebedev Physical Institute of RAS. The experimental part of the work was supported jointly by the Russian Foundation for Basic Research (Grant No. 17-52-10015) and The Royal Society (Grant No. IEC\R2\170217), and by Russian Foundation for Basic Research (Grant No. 20-02-00938). A.M.K. acknowledges a support of Russian Science Foundation (Grant No. 20-42-04405). S.L., F.F., and A.R. were supported in part by the U.S. Army Research Laboratory and the U.S. Army Research Office under Contract No. W911NF-15-1-0448.

APPENDIX

The equation for relative changes in the electric field reflectivity in the presence of the dynamical strain in the film may be written in the form [44]

$$\frac{\Delta r(t)}{r_0} = \frac{4\pi i u(t)}{\lambda} + 2i\left\{A_N\left[(N+P)\int_0^l \varepsilon(t,z)dz + \frac{1}{2}P\int_0^l \varepsilon(t,z)\left(r_{12}e^{2ik_1(l-z)} + \frac{1}{r_{12}}e^{-2ik_1(l-z)}\right)dz\right]\right\}, \quad \text{(A1)}$$

where $u(t)$ is the displacement at the free surface of the film and coefficient A_N is given by

$$A_N = 2i\frac{r_{12}\left(1-r_{01}^2\right)}{(r_{01}e^{-ik_1 l}+r_{12}e^{ik_1 l})(e^{-ik_1 l}+r_{12}e^{ik_1 l})}. \quad \text{(A2)}$$

Optical reflectivity of intensity $R = rr^*$, and taking into account that $\Delta R \ll R_0$ one can get

$$\frac{\Delta R(t)}{R_0} = 2\mathrm{Re}\left(\frac{\Delta r(t)}{r_0}\right). \quad \text{(A3)}$$

Substituting Eq. (A1) to Eq. (A3) we get Eq. (3).

[1] F. J. Morin, Oxides Which Show a Metal-To-Insulator Transition at the Néel Temperature, Phys. Rev. Lett. **3**, 34 (1959).

[2] D. Wegkamp and J. StählerSt, Ultrafast dynamics during the photoinduced phase transition in VO_2 Prog. Surf. Sci. **90**, 464 (2015).

[3] T. C. Koethe, Z. Hu, M. W. Haverkort, C. Schüßler-Langeheine, F. Venturini, N. B. Brookes, O. Tjernberg, W. Reichelt, H. H. Hsieh, H.-J. Lin, C. T. Chen, and L. H. Tjeng, Transfer of Spectral Weight and Symmetry Across the Metal-Insulator Transition in VO_2, Phys. Rev. Lett. **97**, 116402 (2006).

[4] Y. Zhao, J. Hwan Lee, Y. Zhu, M. Nazari, C. Chen, H. Wang, A. Bernussi, M. Holtz, and Z. Fan, Structural, electrical, and terahertz transmission properties of VO_2 thin films grown on c-, r-, and m-plane sapphire substrates, J. Appl. Phys. **111**, 053533 (2012).

[5] H. W. Verleur, A. S. Barker, and C. N. Berglund, Optical properties of VO_2 between 0.25 and 5 eV, Phys. Rev. **172**, 788 (1968).

[6] V. Eyert, The metal-insulator transitions of VO_2: A band theoretical approach, Annalen der Physik **11**, 650 (2002).

[7] K. Okimura and J. Sakai, Changes in lattice parameters of VO_2 films grown on c-plane Al_2O_3 substrates across metal–insulator transition, Jpn. J. Appl. Phys. **48**, 045504 (2009).

[8] A. Cavalleri, C. Tóth, C. W. Siders, J. A. Squier, F. Ráksi, P. Forget, and J. C. Kieffer, Femtosecond Structural Dynamics in VO_2 During an Ultrafast Solid-Solid Phase Transition, Phys. Rev. Lett. **87**, 237401 (2001).

[9] G. R. Khan and B. A. Bhat, Quantum size effect across semiconductor-to-metal phase transition in vanadium dioxide thin films, Micro Nano Lett. **10**, 607 (2015).

[10] A. Joushaghani, J. Jeong, S. Paradis, D. Alain, J. S. Aitchison, and J. K. S. Poon, Wavelength-size hybrid Si-VO_2 waveguide electroabsorption optical switches and photodetectors, Opt. Express **23**, 3657 (2015).

[11] W. R. Roach, Holographic storage in VO_2, Appl. Phys. Lett. **19**, 453 (1971).

[12] U. Koch, C. Hoessbacher, A. Emboras, and J. Leuthold, Optical memristive switches, J. Electroceram. **39**, 239 (2017).

[13] V. Y. Prinz, S. V. Mutilin, L. V. Yakovkina, A. K. Gutakovskii, and A. I. Komonov, A new approach to the fabrication of VO_2 nanoswitches with ultra-low energy consumption, Nanoscale **12**, 3443 (2020).

[14] A. Rúa, F. E. Fernández, and N. Sepúlveda, Bending in VO_2-coated microcantilevers suitable for thermally activated actuators, J. Appl. Phys. **107**, 074506 (2010).

[15] R. Cabrera, E. Merced, N. Sepúlveda, and F. E. Fernández, Dynamics of photothermally driven VO_2-coated microcantilevers, J. Appl. Phys. **110**, 094510 (2011).

[16] T. Wang, D. Torres, F. E. Fernández, C. Wang, and N. Sepúlveda, Maximizing the performance of photothermal actuators by combining smart materials with supplementary advantages, Sci. Adv. **3**, e1602697 (2017).

[17] J. Zhou, Y. Gao, Z. Zhang, H. Luo, C. Cao, Z. Chen, L. Dai, and X. Liu, VO_2 thermochromic smart window for energy savings and generation, Sci. Rep. **3**, 3029 (2013).

[18] M. D. Goldflam, T. Driscoll, B. Chapler, O. Khatib, N. Marie Jokerst, S. Palit, D. R. Smith, B.-J. Kim, G. Seo, H.-T. Kim, M. D. Ventra, and D. N. Basov, Reconfigurable gradient index using VO_2 memory metamaterials, Appl. Phys. Lett. **99**, 044103 (2011).

[19] J.-H. Shin, K. Moon, E. S. Lee, I.-M. Lee, and K. H. Park, Metal-VO_2 hybrid grating structure for a terahertz active switchable linear polarizer, Nanotechnology **26**, 315203 (2015).

[20] E. P. J. Parrott, C. Han, F. Yan, G. Humbert, A. Bessaudou, A. Crunteanu, and E. Pickwell-MacPherson, Vanadium dioxide devices for terahertz wave modulation: a study of wire grid structures, Nanotechnology **27**, 205206 (2016).

[21] I. A. Mogunov, S. Lysenko, A. E. Fedianin, F. E. Fernández, A. Rúa, A. J. Kent, A. V. Akimov, and A. M. Kalashnikova, Large non-thermal contribution to picosecond strain pulse generation using the photo-induced phase transition in VO_2, Nat. Commun. **11**, 1690 (2020).

[22] Z. Yang, C. Ko, and S. Ramanathan, Oxide electronics utilizing ultrafast metal-insulator transitions, Annu. Rev. Mater. Res. **41**, 337 (2011).

[23] Y. Ke, S. Wang, G. Liu, M. Li, T. J. White, and Y. Long, Vanadium dioxide: The multistimuli responsive material and its applications, Small **14**, 1802025 (2018).

[24] D. Maurer, A. Leue, R. Heichele, and V. Müller, Elastic behavior near the metal-insulator transition of VO_2, Phys. Rev. B **60**, 13249 (1999).

[25] H. Dong and H. Liu, Elastic properties of VO_2 from first-principles calculation, Solid State Commun. **167**, 1 (2013).

[26] J. D. Budai, J. Hong, M. E. Manley, E. D. Specht, C. W. Li, J. Z. Tischler, D. L. Abernathy, A. H. Said, B. M. Leu, L. A. Boatner, R. J. McQueeney, and O. Delaire, Metallization of vanadium dioxide driven by large phonon entropy, Nature **515**, 535 (2014).

[27] E. Abreu, S. N. Gilbert Corder, S. J. Yun, S. Wang, J. G. Ramírez, K. West, J. Zhang, S. Kittiwatanakul, I. K. Schuller, J. Lu, S. A. Wolf, H.-T. Kim, M. Liu, and R. D. Averitt, Ultrafast electron-lattice coupling dynamics in VO_2 and V_2O_3 thin films, Phys. Rev. B **96**, 094309 (2017).

[28] I. A. Mogunov, F. Fernández, S. Lysenko, A. J. Kent, A. V. Scherbakov, A. M. Kalashnikova, and A. V. Akimov, Ultrafast Insulator-Metal Transition in VO_2 Nanostructures Assisted by Picosecond Strain Pulses, Phys. Rev. Appl. **11**, 014054 (2019).

[29] O. B. Wright, B. Perrin, O. Matsuda, and V. E. Gusev, Ultrafast carrier diffusion in gallium arsenide probed with picosecond acoustic pulses, Phys. Rev. B **64**, 081202(R) (2001).

[30] O. B. Wright, Ultrafast nonequilibrium stress generation in gold and silver, Phys. Rev. B **49**, 9985 (1994).

[31] T. Saito, O. Matsuda, and O. B. Wright, Picosecond acoustic phonon pulse generation in nickel and chromium, Phys. Rev. B **67**, 205421 (2003).

[32] P. Etchegoin, J. Kircher, M. Cardona, C. Grein, and E. Bustarret, Piezo-optics of GaAs, Phys. Rev. B **46**, 15139 (1992).

[33] C. He, O. Ristow, M. Grossmann, D. Brick, Y. Guo, M. Schubert, M. Hettich, V. Gusev, and T. Dekorsy, Acoustic waves undetectable by transient reflectivity measurements, Phys. Rev. B **95**, 184302 (2017).

[34] C. Thomsen, H. T. Grahn, H. J. Maris, and J. Tauc, Surface generation and detection of phonons by picosecond light pulses, Phys. Rev. B **34**, 4129 (1986).

[35] O. Matsuda, M. C. Larciprete, R. Li Voti, and O. B. Wright, Fundamentals of picosecond laser ultrasonics, Ultrasonics **56**, 3 (2015).

[36] S. Lysenko, V. Vikhnin, F. Fernandez, A. Rua, and H. Liu, Photoinduced insulator-to-metal phase transition in VO_2 crystalline films and model of dielectric susceptibility, Phys. Rev. B **75**, 075109 (2007).

[37] V. Théry, A. Boulle, A. Crunteanu, J. C. Orlianges, A. Beaumont, R. Mayet, A. Mennai, F. Cosset, A. Bessaudou, and M. Fabert, Role of thermal strain in the metal-insulator and structural phase transition of epitaxial VO_2 films, Phys. Rev. B **93**, 184106 (2016).

[38] T.-H. Yang, R. Aggarwal, A. Gupta, H. Zhou, R. J. Narayan, and J. Narayan, Semiconductor-metal transition characteristics of VO_2 thin films grown on c- and r-sapphire substrates, J. Appl. Phys. **107**, 053514 (2010).

[39] G. Tas and H. J. Maris, Electron diffusion in metals studied by picosecond ultrasonics, Phys. Rev. B **49**, 15046 (1994).

[40] A. V. Scherbakov, P. J. S. van Capel, A. V. Akimov, J. I. Dijkhuis, D. R. Yakovlev, T. Berstermann, and M. Bayer, Chirping of an Optical Transition by an Ultrafast Acoustic Soliton Train in a Semiconductor Quantum Well, Phys. Rev. Lett. **99**, 057402 (2007).

[41] H.-Y. Hao and H. J. Maris, Experiments with acoustic solitons in crystalline solids, Phys. Rev. B **64**, 064302 (2001).

[42] P. van Capel, E. Péronne, and J. Dijkhuis, Nonlinear ultrafast acoustics at the nano scale, Ultrasonics **56**, 36 (2015).

[43] A. Akimov, E. Young, J. Sharp, V. Gusev, and A. Kent, Coherent hypersonic closed-pipe organ like modes in supported polymer films, Appl. Phys. Lett. **99**, 021912 (2011).

[44] V. Gusev, Laser hypersonics in fundamental and applied research, Acustica **82**, S37 (1996).

[45] M. Currie, M. A. Mastro, and V. D. Wheeler, Characterizing the tunable refractive index of vanadium dioxide, Opt. Mater. Express **7**, 1697 (2017).

[46] Y.-C. Wen, C.-L. Hsieh, K.-H. Lin, H.-P. Chen, S.-C. Chin, C.-L. Hsiao, Y.-T. Lin, C.-S. Chang, Y.-C. Chang, L.-W. Tu, and C.-K. Sun, Specular Scattering Probability of Acoustic Phonons in Atomically Flat Interfaces, Phys. Rev. Lett. **103**, 264301 (2009).

[47] B. Lazarovits, K. Kim, K. Haule, and G. Kotliar, Effects of strain on the electronic structure of VO_2, Phys. Rev. B **81**, 115117 (2010).

[48] O. Matsuda, O. B. Wright, D. H. Hurley, V. Gusev, and K. Shimizu, Coherent shear phonon generation and detection with picosecond laser acoustics, Phys. Rev. B **77**, 224110 (2008).

[49] A. B. Pevtsov, D. A. Kurdyukov, V. G. Golubev, A. V. Akimov, A. A. Meluchev, A. V. Sel'kin, A. A. Kaplyanskii, D. R. Yakovlev, and M. Bayer, Ultrafast stop band kinetics in a three-dimensional opal-VO_2 photonic crystal controlled by a photoinduced semiconductor-metal phase transition, Phys. Rev. B **75**, 153101 (2007).